Scientia Iranica B (2023) 30(2), 428–441

Sharif University of Technology
Scientia Iranica
Transactions B: Mechanical Engineering
http://scientiairanica.sharif.edu

Investigating the effect of train speed and ground clearance on aerodynamics of a simplified high-speed train

S. Norouzi[a], S. Hossainpour[a,*], and M.M. Rashidi[b]

a. *Department of Mechanical Engineering, Sahand University of Technology, Tabriz, Iran.*
b. *University of Electronic Science and Technology of China, Chengdu, 610054, Sichuan, PR China.*

Received 23 May 2022; received in revised form 15 July 2022; accepted 1 October 2022

KEYWORDS
Aerodynamic forces;
Ground clearance;
High-speed train;
Stability;
Fluid flow.

Abstract. The present paper investigates the effect of train speed and ground clearance on aerodynamic forces of a simplified high-speed train. For this purpose, 20 different cases including trains with five different speeds and four varied ground clearances were numerically simulated. The results showed that increasing the train speed had a dual effect on increasing the vertical upward lift forces. Non-dimensional ground clearances above than 0.22 at speeds above 250 km/h resulted in dramatic upward lift forces and led to train instability. At ground clearances below than 0.092, a rise in the speed increased the downward force, enhancing the stability of the train. Moreover, further analysis of the ground clearance effect demonstrated that at a ground clearance equal to about 0.048, the lift force remained approximately constant at different train speeds. The air velocity profiles for the train experienced a dimensionless rise with increase in the value of ground clearance, except for the front part of the train. This increase was precisely apparent at a speed of 350 km/h and resulted in a 29% increase in the air velocity along the sections below the train. This rise in speed may disrupt the balance of passengers and pedestrians as well as workers around the train.

1. Introduction

One of the imperative design items for a train is the aerodynamic force exerted on the train body due to the change of flow lines. The flow around a train would generally undergo a large-scale separation, resulting in large aerodynamic forces and much instability [1–4]. In the prevailing era, several designers and developers in this industry are focused on simulating and creating an optimal design to deal with aerodynamic flows. Due to the complicated geometry and the existence of turbulent flow structures at different dimensions, the flow around the train is characterized by much complexity, including high curvature of the flow near the wall, non-isotropic turbulent flow, and velocity and pressure fluctuations in air collision with the car wall [5–8]. This makes numerical simulation challenging with most of turbulence models. Numerous numerical studies have been performed in this field. In [9], the Large Eddy Simulation (LES) method was used to simulate reverse wind flow facing a simple high-speed train model, considering different profiles of train heads at a Reynolds number of 3×10^5. In this 3D analysis, the effects of changes in train head shapes on some aerodynamic parameters such as drag and lift forces

*. *Corresponding author.*
E-mail address: hossainpour@sut.ac.ir (S. Hossainpour)

doi: 10.24200/sci.2022.60478.6817

and the field of pressure and speed were investigated. In [10], the experimental and numerical methods were employed to simulate and analyze the vortex flow and the boundary layer around the head and end of a high-speed train.

In [11], the LES method was applied to simulate the air flow passing through a stationary cargo train. In this study, in order to analyze aerodynamic performance, a 1:20 ratio model of a high-speed train with two wagons and a Reynolds number of 2×10^5 was simulated. Transverse loads on wagons, drag, and lift forces were the most important findings of this research. Yang et al. [9] employed the LES method to simulate the air pressure around a high-speed train. In this investigation, a simplified model of a high-speed train with five wagons with a ratio of 1:20 was considered, and the vortex flow, boundary layer, and air velocity around the train were analyzed as the most substantial parameters.

Johnson et al. [12] deployed a PIV laboratory method in a water towing tank to evaluate the flow velocity profile under the train in three modes with cavities and bogies on the train floor and without them for a 1:50 scale high-speed general train model. In their study, the Reynolds number for the train was considered 0.24×10^6. In [13], authors compared the numerical method (Reynolds-Averaged Navier-Stokes (RANS)) with laboratory results considering a wind tunnel on the pressure exerted on a high-speed train. Li et al. [14] examined the flying ballast phenomenon for a high-speed train with real dimensions at 350 km/h. Their study aimed to analyze the effects of the ballast height, stone shape in the upper layer of the ballast, and the ballast bed compaction on the problem. In [15], the numerical method Fast Fluid Dynamics (FFD) was utilized to assess the performance of aerodynamic characteristics and their optimization, including drag and lift forces on a high-speed train. Air flow in this study was considered three-dimensional, incompressible, stable, and viscous. In [16], the aerodynamic performance of a high-speed train was simulated and analyzed using Detached Eddy Simulation (DES) of the computational fluid dynamics and fluent software. They investigated the effects of both stationary and moving grounds in their numerical setup. They concluded that the total drag of the train was higher under moving ground conditions than that under stationary ground conditions.

Niu et al. [17] evaluated the Unsteady Reynolds-Averaged Navier-Stokes (URANS), Scale-Adaptive Simulation (SAS), and DES turbulence models to simulate the flow around the Inter-City-Express 3 (ICE3) high-speed train and investigated the performance of each of these methods and their differences. They concluded that the computational cost of SAS and DES models was 10 to 20 times greater than that of the URANS method. Nonetheless, the mentioned authors demonstrated that the unsteady $k-\omega$ SST model had a remarkable ability to estimate the aerodynamic coefficients of lift and drag. Hence, they suggested that this method be utilized rather than costly ones in those studies that focus on lift and drag coefficients. In [18], a comparison between stationary and moving trains with and without a windbreak wall under the cross-wind effect was made using numerical simulations. In the above survey, they examined the pressure distribution as well as the speed and forces applied on the high-speed train. Another study [19] numerically analyzed the aerodynamic characteristics of high-speed trains with different nose lengths. They assessed the effect of the train nose length on the drag and lift forces applied to the tail vehicle. They revealed that the lift force of the head car was stronger than the effect on other cars, and when the length of the train nose increased, the C_d value of the tail car was reduced by 30.53% and the C_l value of the head car increased by 87.98%.

In [20], cross-wind flows on high-speed trains in two-track rails with porous protection were analyzed. The simulation method utilized was the Lattice-Boltzmann method. In [21], numerical and experimental methods were applied to assess the coefficients of aerodynamic forces of rail vehicles on a hill with a specific geometry. Despite a somewhat considerable number of experimental and numerical studies performed on aerodynamic forces on high-speed trains, few studies have been conducted to determine and assess the distance from the train's floor to the ground (ground clearance). Researchers in [22,23] attempted to determine the effect of ground clearance on aerodynamic forces. In the mentioned study, given the application of the Improved Delayed Detached Eddy Simulation (IDDES) method and its high computational cost, the speed of a high-speed train was considered 50 km/h. However, the effect of different train speeds on aerodynamic forces has not been completely investigated in their study.

The present survey investigates the effect of the ground clearance and speed of the train in the simplified ICE3 high-speed train model on aerodynamic coefficients. Meanwhile, it is notable that this type of train is currently used in various parts of Europe and China. Given the fact that the speed of ICE 3 high-speed trains ranges from 200 to 350 km/h, five speeds of 50, 150, 200, 250, and 350 km/h, and four ground clearances of 0.048, 0.092, 0.136, and 0.22 are taken into consideration in this study.

2. Method

2.1. Turbulence modeling

RANS are typical models of turbulence problems. In

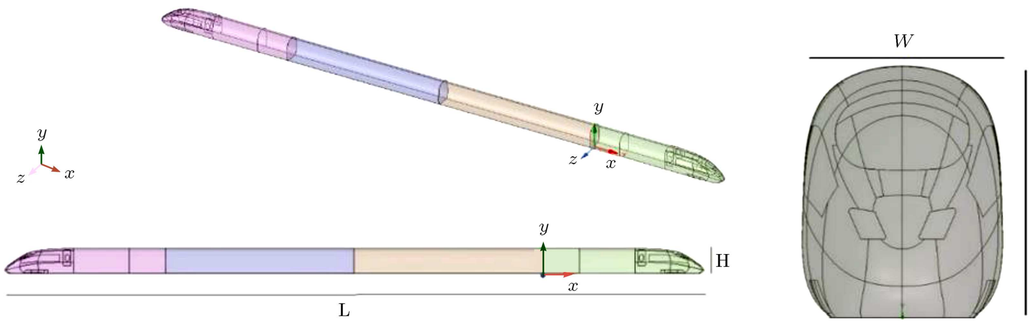

Figure 1. Trimetric views, front and side of the ICE3 express train.

this model, variables are discretized into two sections of fluctuating and mean components. Adding variables to Navier-Stokes equations and averaging them will generate averaged Navier-Stokes equations.

By keeping time derivative terms of the velocity constant, we will have the equation containing an ensemble of turbulent flow states of unsteady RANS model. Mean velocity and pressure are represented as follows [24,25]:

$$\frac{\partial \bar{u}_i}{\partial \bar{x}_i} = 0, \tag{1}$$

$$\frac{\partial \bar{u}_i}{\partial t} + \bar{u}_j \frac{\partial \bar{u}_i}{\partial \bar{x}_j} = -\frac{1}{\rho}\frac{\partial \bar{p}}{\partial \bar{x}_i} + \frac{\partial}{\partial \bar{x}_j}\left(\nu \frac{\partial \bar{u}_i}{\partial \bar{x}_j}\right) + \frac{1}{\rho}\frac{\partial \tau_{i,j}}{\partial \bar{x}_i}, \tag{2}$$

where $\tau_{ij} = \overline{\acute{u}_l \acute{u}_j}$ is the Reynolds stress tensor, which cannot be determined in terms of mean flow variables. However, some turbulent flow models have been developed to predict it better. Most of these models use more equations for estimating Reynolds stress in terms of mean flow gradient by changing turbulent viscosity, according to local turbulent time, velocity, and length scales. Some auxiliary equations of kinetic energy per unit mass (k) and equation of turbulent dissipation (ε) must be solved coupled with these equations. However, to the best of the authors' knowledge, it is possible that the $k-\omega$ SST shear stress transfer model be used to match the turbulence model with the desired geometry and conditions. This model exhibited good performance in dealing with similar problems of surface pressure analysis on high-speed trains [26,27]. Classical $k-\varepsilon$ model has better performance in predicting free flow out of the boundary layer, while classical $k-\omega$ is known as the best for predicting flow behavior near the wall and boundary layer. To benefit the accuracy and reliability of both, we must synthesize $k-\varepsilon$ and classical $k-\omega$ models. The answer comes in the form of $k-\omega$ SST. This model is one of the best URANS models that predicts large-scale separation phenomenon and it is the recommended model of wake flow capture in high-speed trains [28].

2.2. Train geometry

Previous works [3,29–32] presented the model of train and its geometry (see, Figure 1). In this study, a simplified 1:10 model of the Bahn ICE3 high-speed train is used, which includes four cabins whose length (L), width (W), and height (H) are equal to 10.14, 29, and 0.36 m, respectively. Recent studies on high-speed trains have found that the effect of wheels on aerodynamic forces can be ignored [33,34]. In this research, four dimensionless distances of train floor to the ground, (h/H) of 0.22, 0.136, 0.092, 0.048, have been considered to evaluate the impact of ground clearance on aerodynamic forces.

2.3. Computational domain and boundary conditions

The computational domain considered is a rectangular space with the following dimensions: 97 W length, 20 W height, and 40 W width. It is considered wide enough to ensure that boundary conditions would not affect the flow structures around the train. Figure 2 shows the geometry and boundary conditions of the solution domain.

The upper boundary and the lateral boundaries are considered symmetric [35]. To simulate the relative velocity between the train and the ground, the ground boundary condition is considered as a wall with a velocity of free flow (moving ground and fixed train condition). The front nose position of the train is located at a distance of 10 W from the entrance boundary of the domain, as illustrated in Figure 2. The boundary condition at the output is set as constant zero static pressure. The distance from the end of the train to the output border is 52 W, which is intended to investigate the vortex structures behind the train and ignore the effect of the pressure boundary condition at the output.

The input boundary condition is uniform velocity throughout the entrance surface. The characteristic length (train height) 0.294 m, air density (ρ) 1.184 kg/m^3, and viscosity 1.855×10^{-5} kg/ms are considered in all cases. The turbulence intensity of 1% was assumed at the inlet to simulate the free stream condition with low turbulence inside the experimental wind tunnel setup. These specifications are mainly intended for confirmation in accordance with previous experimental data.

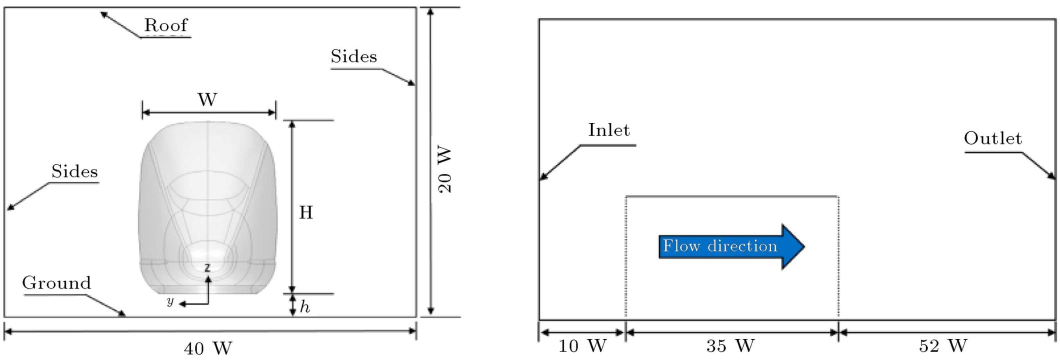

Figure 2. Solution domain and boundary conditions.

2.4. Meshing strategy

The domain mesh is generated using a predominately Cartesian cut-cell approach. This approach generates a higher mesh concentration near the body and wake region for a more detailed prediction and lowers smoothly as it goes away from the body and ground level. The computational mesh has been generated using GridPro software and imported into OpenFOAM open-source code. Due to the large gradients in the two areas next to the train and the ground clearance, these areas have been subdivided using two separate blocks.

The use of a micro mesh requires the application of an advanced computing system, and it will certainly be costly. To study the independency of the solution from the network, a variable like speed, pressure, or drag coefficient should be chosen first and studied in different networks in order to achieve optimal result with the minimum number of networks. In other words, in the first step, the simulation is done with a relatively light network and the desired variables are extracted. Considering that the objective is to choose the most optimal size for gridding, the number of grids should be determined to obtain simulation results so that the computational cost would not increase.

The cells have grown in a proportion less than 0.1 from the train's surface to the outermost regions. Given the use of unsteady URANS turbulence models as well as the wall function near solid boundaries in this section, the cells near the buckets are arranged such that y^+ value be considered around 30 to 100 in different areas, especially in the area of the train tip, which is a stagnation point. Figure 3 shows the grid on the surface and near the ground.

In this simulation, three different refined grids, i.e., coarse, medium, and fine, are assessed, focusing on keeping similar compression factors between meshes. These three grids are considered to achieve better and higher accuracy and they represent the above-mentioned critical regions of grid independency.

To consider all the main flow features, the dimensions of refinement regions were evaluated according to preliminary simulations.

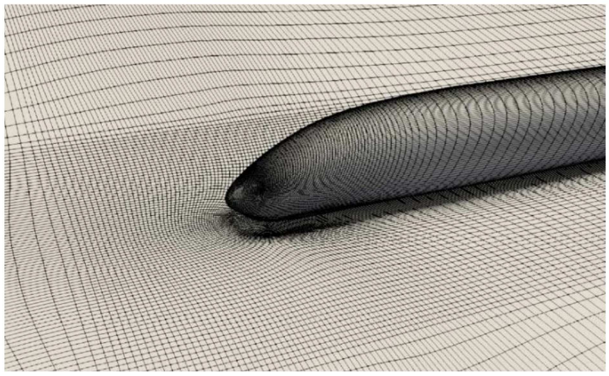

Figure 3. Surface meshing system.

3. Results

The numerical solver utilized in the current paper is the open-source code OpenFOAM 7.0. In order to study velocity and pressure and determine the vortices and turbulences around and behind the train, more precisely, the unsteady URANS $k-\omega$ SST model is employed. Time step is considered so that the CFL number can be less than 0.9. In this way, the time step in each step is calculated, which is estimated to be approximately equal to $\Delta t = 10^{-4}$ s for most time steps. Therefore, wall-functions based on the $k-\omega$ SST implemented in OpenFOAM were utilized to model the near-wall behavior of turbulence. Simulations were carried out for all cases using the incompressible, transient PimpleFOAM solver.

3.1. Validation

The approximate time for convergence in each time step for the second computing mesh is about 50 to 90 s for each processor with a processing power of 3.7 MHz. Given that unsteady URANS models are used in this simulation, we need to ensure a sufficient solution time to accurately estimate average flow variables such as average velocity field and pressure. Otherwise, the average flow fields may not be estimated correctly. For this purpose, Figure 4 shows the value of the total drag coefficient on the whole train from zero to 8 seconds. As can be seen, 5 s is sufficient to achieve the convergence

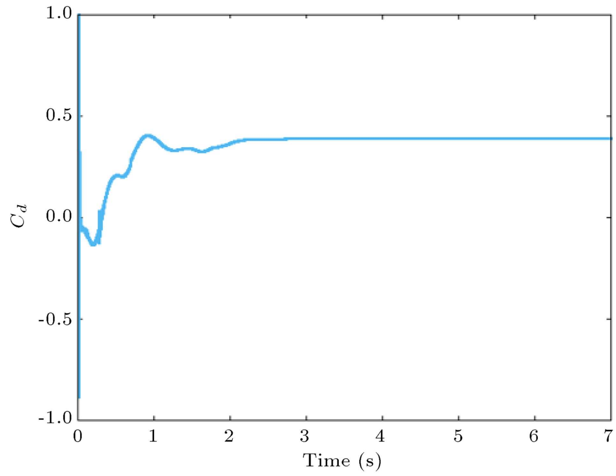

Figure 4. Total drag coefficient on the train from the beginning of the solution up to 7 s.

of the average flow quantities. All average quantities in this paper are reported from 5 to 15 s to ensure the accuracy of the averaging operation. It was observed that averaging in time periods longer than 15 s would not make a considerable difference in the results of the velocity and pressure fields.

In order to investigate the solution independence from the computational grid, 3 different computational grid sizes were used for the unsteady $k-\omega$ SST model. The meshing strategy described is the same for all the three grids, but the number of computational cells is 4 million, 6.2 million, and 9 million cells for Grid 1, Grid 2, and Grid 3, respectively. Figure 5(a) shows the horizontal velocity profile at a distance below the train to the ground at $x = 0.08$ m, and Figure 5(b) shows the vertical velocity of the air flow in the area behind the train at $x = 10$ m. These speed profiles are drawn at a train speed of 250 km/h as well as the ground distance from the train floor equal to h_1. For the rest of the cases, the solution grid independence was examined.

According to Figure 5, the results of the average horizontal and vertical velocities for the medium and fine grids are significantly close to each other at different sections; therefore, it can be concluded that further thinning of the grid will not affect the solution.

As illustrated in Figure 6, the friction component of the drag coefficient calculated by the coarse mesh is 45% less than the drag coefficient in the fine mesh, whereas the difference between the medium and fine meshes is less than 4%. Furthermore, for the pressure component of the lift coefficient, the difference between coarse and fine meshes is about 30% and for medium and fine meshes, it is roughly 5%. Considering all the comparisons mentioned above and other comparisons

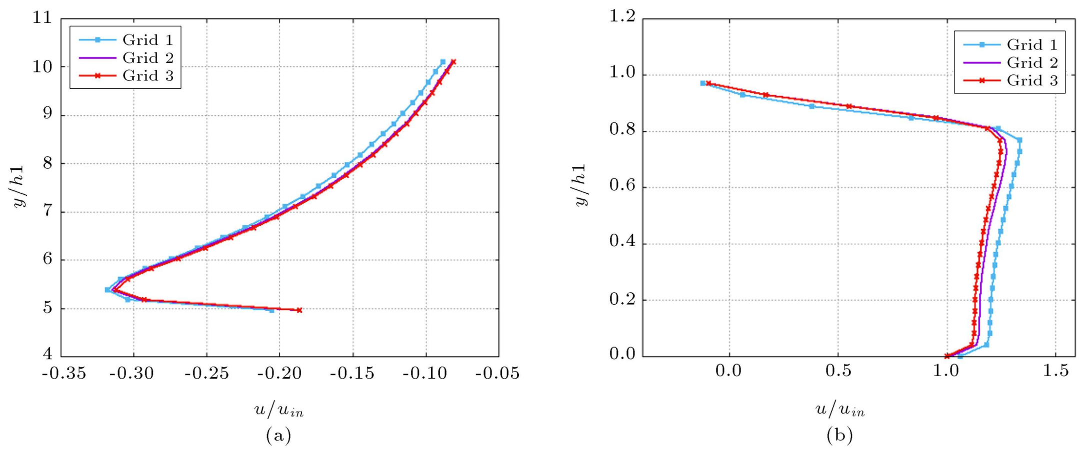

Figure 5. Effect of mesh grid cell number on velocity profile along various sections: (a) Horizontal velocity below the train at $x = 0.08$ ml and (b) vertical velocity behind the train at $x = 10$ m.

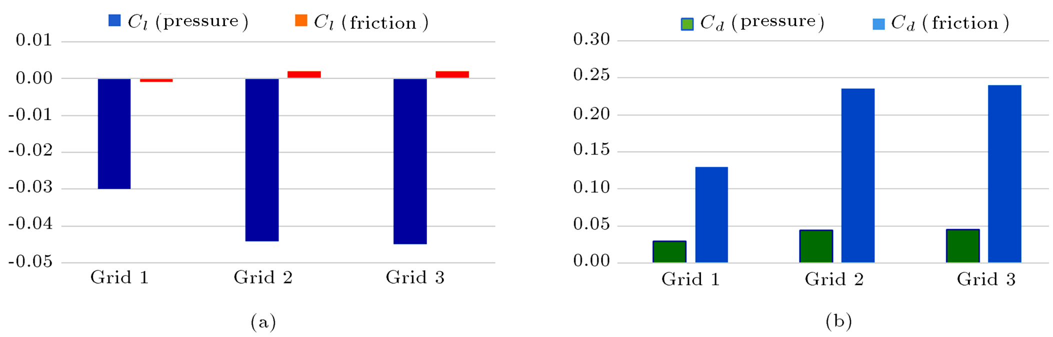

Figure 6. Comparison of friction and pressure components of lift coefficient determined by different networks.

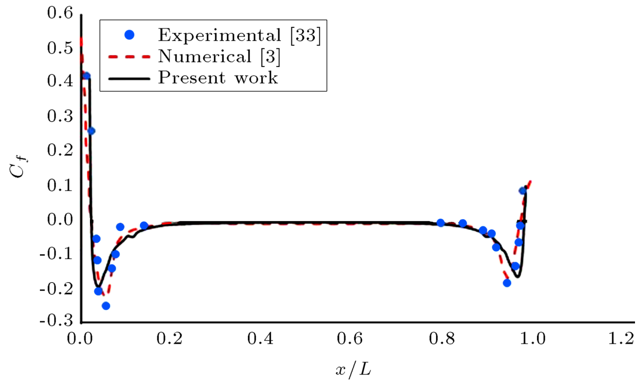

Figure 7. Comparison of pressure coefficient of the present work with laboratory data [33] and numerical simulation by IDDES method [3].

made for all speeds (not presented here for the sake of brevity), most of the simulations in this paper utilize a 6.2 M cell mesh.

Figure 7 shows the comparison of the simulation pressure coefficient of the present work with the experimental data obtained in [33] and the numerical simulation in [3].

Dong et al. [3] studied the geometry of ICE3 and used the LES and RANS hybrid turbulence methods with the help of the IDDES (combination of DDES model and the LES wall model). Using nearly 29 million computational cells accompanied by a huge computational cost, researchers in [3] managed to study the flow around the train as well as the forces on the train. In [36], the wind tunnel was used to study the underbody velocity profile of the ICE3 train irrespective of the effect of lateral winds. However, in their study, the Reynolds number is considered 1.65×10^6, which is somewhat different from the Reynolds number used in this study. Therefore, experimental data are slightly different from the simulations of the present study and those in [3]. However, the pressure coefficient for the train is qualitatively consistent with the laboratory results.

3.2. Aerodynamics coefficients

Figure 8 illustrates the friction and pressure components of the drag (Figure 8(a)) and lift (Figure 8(b)) aerodynamic coefficients for different train speeds and four different ground clearances. In all the diagrams related to drag coefficients, it can be easily observed that the contribution of the friction component to the pressure component is multiplied because of the aerodynamic shapes of the train head and the high train length. As observed in the lift coefficient diagrams at all ground clearances, the drag coefficients decrease as the train speed rises. This reduction functions in such a way that the deceleration becomes more significant at lower speeds (50 and 150 km/h), and as we move towards higher speeds, this deceleration reduces as the drag coefficient decreases. In this way, particularly at short ground clearances (h_2 and h_3), the values of drag coefficients remain constant. Thus, the speed of 250 km/h can be considered critical to keeping the drag coefficient constant, given the curvature of the graph and, also, a difference of less than 5% in the total drag coefficient at the last two speeds.

Another striking point is that at a speed of 50 km/h and a distance of h_0, the maximum amount of drag equal to 0.421 occurs in all the cases. As the ground clearance decreases at this speed, C_d gradually decreases to 0.385 at time h_3, which is equivalent to a reduction of 8.6%. However, at high speeds, the effect of ground clearance on the drag coefficient is highly inconsequential. For instance, at a speed of 350 km/h and in the case of h_0, the value of C_d is 0.267; in the case of h_3, its value is equal to 0.262, indicating a slight 1.8% variation. The reason for the above matter is illustrated in Figure 9(a), in which the effect of pressure and frictional forces on the drag coefficient at different ground clearances remains nearly constant.

The ratio of different components of the lift coefficient is quite the opposite of that of the drag coefficient (Figure 8(b)). As clearly shown in Figure 8, frictional forces generate a force on the positive vertical axis (positive lift coefficient), thus deteriorating the train stability. In contrast, the pressure components of the lift forces, which are several times greater than the frictional component, exert a downward force that enhances the train stability.

We managed to derive an important point from investigating the effect of the train's ground clearance on its stability. As shown in Figures 8, at short distances (h_2 and h_3), as the train speed increases, the lift coefficient gradually rises, and this rise continues up to 250 km/h. Next, as the flow velocity under the train increases at distances h_2 and h_3 and the pressure below the train decreases, the vertical forces in the opposite direction of the vertical axis (towards the ground) are intensified. Consequently, the lift force becomes more negative, thus facilitating the stability of the train on the move. Thus, increasing the train speed up to 350 km/h at these two distances will not raise the instability of the train. Nevertheless, according to the lift coefficient diagrams in the two cases of h_1 and h_0, it is observed that the lift force rises if the train speeds up. However, in the case of h_1, the lift coefficient appears to remain around -0.04, while in the case of h_0, as the speed increases, a significant increase in the magnitude of vertical forces can be seen in the upward direction, such that at a speed of 350 km/h, C_l reaches -0.003. Therefore, given the shape of the curve and the value of C_l (Figure 8(b)), it seems not to be in the stable range. This issue can be quite hazardous when the wind blows or passes through different tunnels. Besides the points mentioned above, based on the comparison of the lift

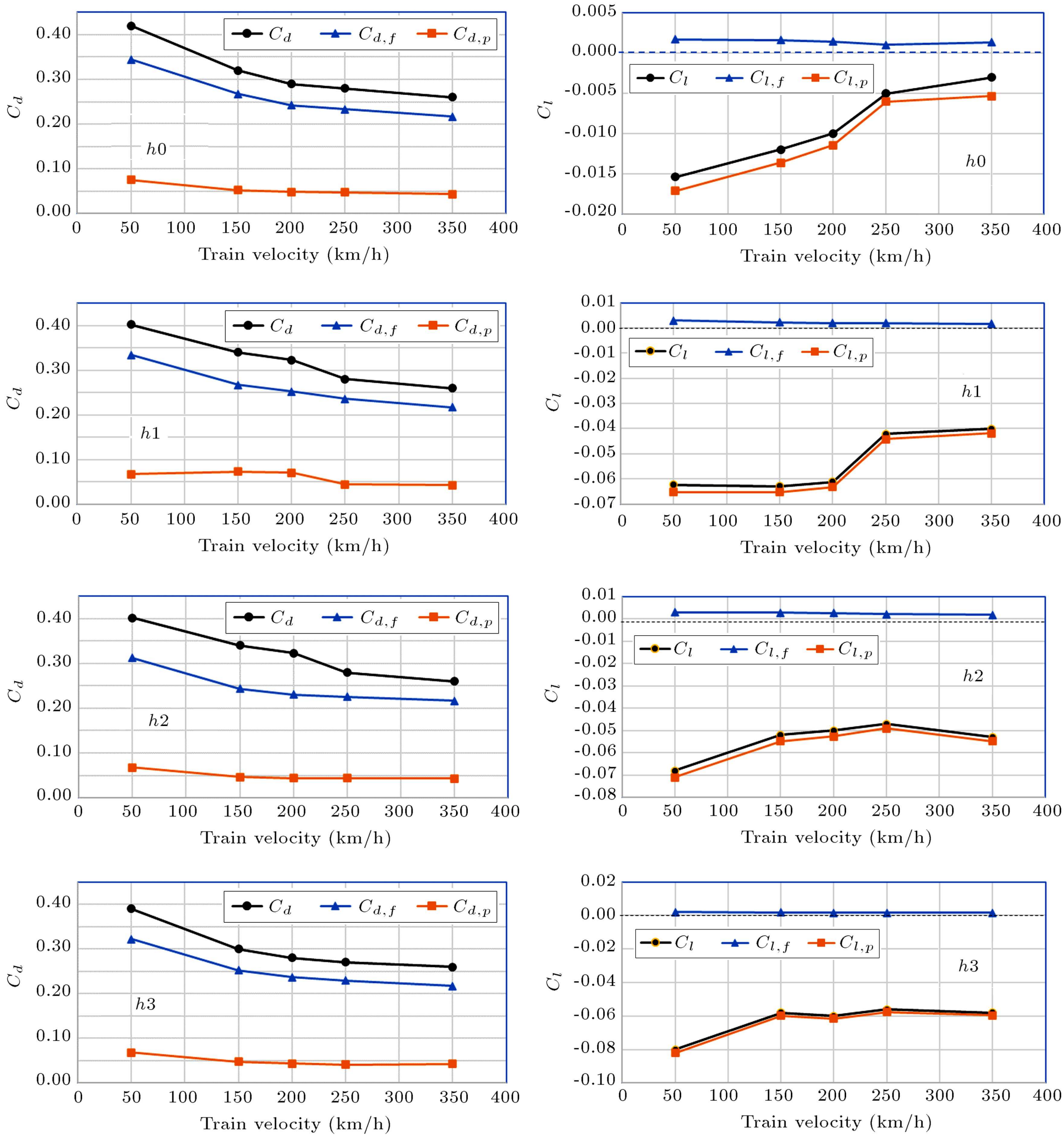

(a) (b)

Figure 8. Friction and pressure components of (a) (left column) drag coefficients and (b) lift (right column) for ground clearance and different train velocities.

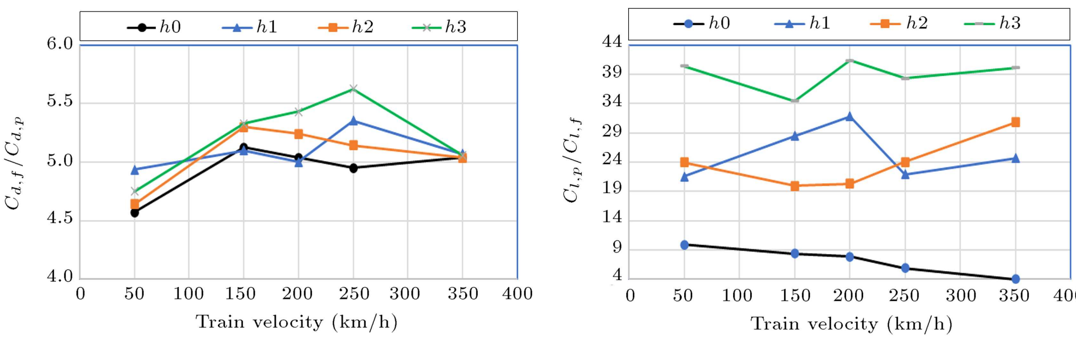

(a) (b)

Figure 9. (a) The ratio of the friction component to the pressure component of the drag coefficient and (b) the ratio of the pressure component to the friction coefficient of the lift coefficient at different velocities and ground clearances.

coefficients at different distances (Figure 8(b)), it is inferred that as the ground clearance rises, the total lift coefficient decreases gradually. For example, at a speed of 50 km/h for the distance h_3 (as the minimum ground clearance), C_l is equal to -0.08, and for the case h_0, it is equal to -0.0154. Moreover, at 350 km/h, the C_l coefficient for h_3 and h_0 bags is -0.058 and -0.003, respectively.

In general, from the previously mentioned issues, it can be concluded that at a distance of h_0, the drag coefficient does not differ much from other cases (maximum 8.6%). However, by examining the lift coefficient, it becomes apparent that the train gradually loses its stability with increase in its speed, which crosses off the use of this distance as an option. The reason can be attributed to the high air flow rate (compared to h_2 and h_3) under the train, which generates a powerful upward lift force. In the h_1 case, the total lift coefficient is quite desirable at low speeds and the vertical forces are completely downward. However, upon increasing the speed to 250 km/h, the vertical upward forces increase significantly and the lift coefficient decreases to -0.04. Therefore, the application of this distance to a train with high speeds, especially in the presence of cross winds and tunnels as well as other lower and upper parts of the train, necessitates further investigation. The h_2 and h_3 cases present a reliable lift coefficient for a train at all speed rates such that it would not experience any instability as the speed rises in the given range.

Figure 9(a) shows the ratio of the friction component to the pressure component of the drag coefficient, and Figure 9(b) illustrates the ratio of the pressure component to the friction of the lift coefficient at different velocities and ground clearances. As illustrated in Figure 9(a), the ratio of pressure to frictional forces increases slightly with the reduction of the ground clearance (at most speed rates). Nevertheless, not all ratios at different distances and speeds change drastically and almost remain in the range of 4.5 to 5.7 times. Perhaps, since the drag coefficient is highly affected by the frictional forces on the train body, the speed and ground clearance will not significantly affect the drag coefficient. Undoubtedly, the length and area of the body will have a greater effect on the frictional forces and, consequently, the drag coefficient. Figure 9(b) shows the ratio of the pressure component to the friction of the lift coefficient at different speeds and ground clearances. As presented in Figure 9, frictional forces slightly affect the lift coefficient as opposed to pressure forces. As the ground clearance rises, the flow velocity profile under the train flattens and its diffuser effect decreases (Figure 10); thus, the pressure on the train decreases to a lower degree. Hence, the effect of the difference in pressure forces on the top and bottom of the train is reduced and, therefore, the effect of the pressure component of the lift coefficient decreases. As the ground clearance decreases (in cases h_1 and h_2), the ratio of pressure to friction forces fluctuates in the range of 19 to 32, depending on the flow velocity. This is how high and low pressure differences for the train rule over the viscous forces at different speeds. In the case of h_3, at different speeds, this ratio is nearly constant ranging between 34 and 41, implying the complete dominance of the pressure forces applied to the train over the frictional forces.

3.3. Velocity profiles under the train

Figure 10 illustrates the dimensionless horizontal velocity profile by the train speed in terms of ground clearance, which is non-dimensioned utilizing the height h_0 for all ground clearances. It presents for three train speeds 50, 250, and 350 in 3 specified cross-sections (1 (left column), 4 (middle column), and 6 (right column)). This figure presents only three velocities for the sake of brevity and, also, given the high similarity between the dimensionless velocity profiles at various speeds. Section 1 is located just below the front panel of the train. The collision between the air flow and this panel causes the flow to return to this area due to the negative flow velocity. In section 1, the negative dimensionless velocity at different ground clearances is nearly 0.2 (Figure 10, left column).

Another point to consider in the case of section 1 is that as the ground clearance decreases, the train speed increases. Increasing the speed of the train in this area reduces the pressure on the train. As a result, the resulting pressure forces increase in the vertical direction downwards and this effect on increasing the lift coefficient downwards due to the reduction of the distance is observed in Figure 10. By passing through the front panel of the train, the velocity profile becomes irreversible, and as can be seen in sections 4 and 6, with an increase in the ground clearance, the dimensionless horizontal velocity profile becomes irreversible and gradually more expansive.

Figure 11 illustrates the dimensionless velocity profile of the flow under the train for cases h_0 to $h4$ at different velocities and in 6 different sections. The difference between this figure and Figure 10 lies in their non-dimensionalization ways. In Figure 10, all ground clearance heights are made dimensionless using h_0, while in Figure 11, non-dimensionalization is made by their own clearance height.

As shown in Figure 11, sections 1, 2, and 3 are related to the head of the train as section 1 is located under the front panel of the train. In the first three sections, the dimensionless speed profiles are very similar at different speeds. The most significant difference in these profiles is related to the speed of 350 km/h, at which the maximum speed is reported to be slightly

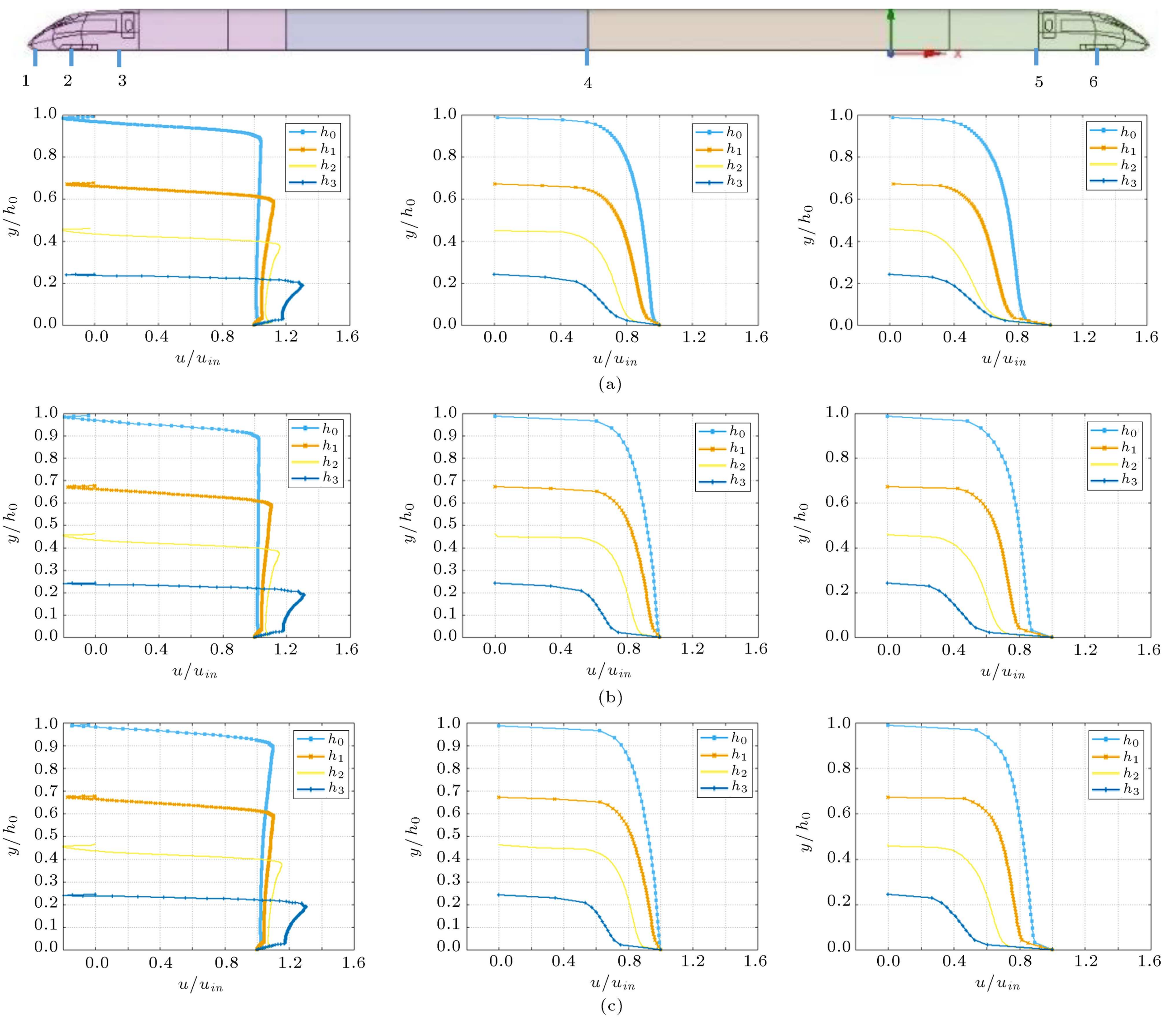

Figure 10. Non-dimensional horizontal flow velocity profile under the train in sections 1 (left column), 4 (middle column), and 6 (right column) and at speeds (a) 50 km/h, (b) 200 km/h, and (c) 350 km/h.

higher than other speeds in all cases. Another striking point that can be observed in the velocity profiles is that as the ground clearance decreases at all speeds, the maximum speed rises and the location of this maximum speed tends toward the ground. For example, the maximum values of dimensionless velocity in section 2 increase from 1.2 in case h_0 to more than 1.4 in case h_3. Another notable point is that in sections 1 and 2, which correspond to the front panel of the train, a negative velocity, which indicates flow reversal, occurs due to the effect of the panel. As shown in section 2, as the ground clearance decreases, the value of the negative dimensionless velocity decreases from -0.23 in the case h_0 to -0.11 in case h_3.

In the middle of the train (section 4), the variation in dimensionless velocities increases with increasing velocity, especially in the ground clearance. In the case of h_0, the average dimensionless speed passing under the train is 50 km/h compared to the train speed, and for speeds of 150, 200, 250, and 350 km/h, it is 4%, 4.4%, 5.5%, and 12% higher, respectively. In the case of h_3, the maximum difference in the average dimensionless speeds, i.e., between the two speeds of 50 and 350 km/h, is 4.3%.

Along the ending part of the train (sections 5 and 6), the difference in speed profiles at different train speeds gradually increases. This is particularly evident in the cases of h_0 and h_1. At the end of the train (section 6) at a speed of 350 km/h, the average dimensionless speed passing under the train in cases h_0, h_1, h_2, and h_3 is 29%, 25%, 24%, and 13% higher than the train speed of 50 km/h, respectively. Increasing the induced speed under the train can upset the balance of pedestrians and railway workers around the tracks. Plus, Ma et al. [36] found that increasing the flow speed under the train would expand the percentage

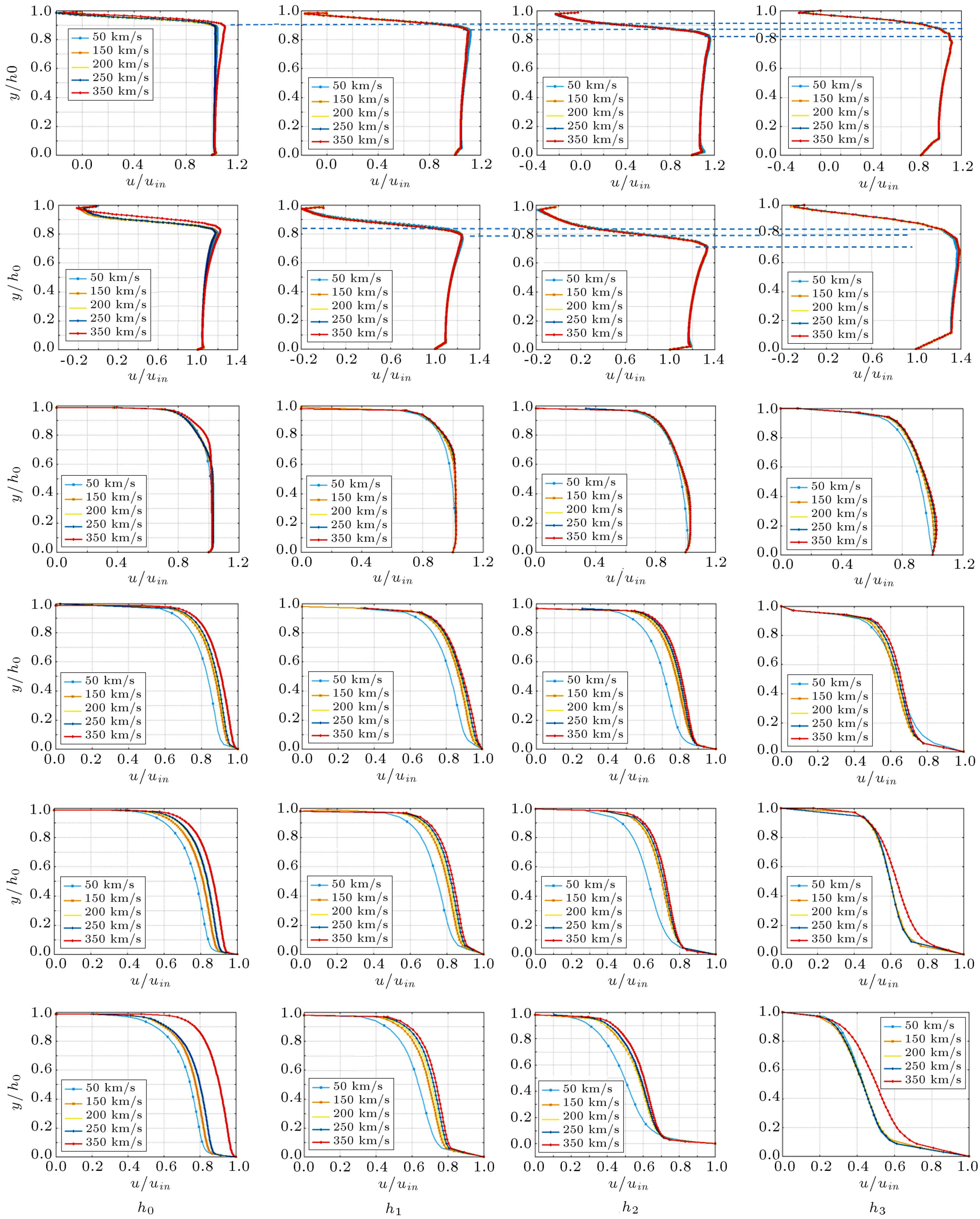

Figure 11. Non-dimensional horizontal flow velocity (u/u_{in}) profile under the train in all cases versus non-dimensional ground clearance height (h/h_i).

of passengers who get on or off the train. Based on Figure 10, with an increase in the train speed to 350 km/h, the maximum speed increases from 8 to 29% in all sections.

Figure 12 reveals the air mass flow rate ratio at the beginning of the train (section 3) to the transient mass flow rate at the end of the train (section 5) $\frac{\dot{m}_5}{\dot{m}_3}$. Reducing the ground clearance affects the flow velocity profile under the train and the air flow around the train. This lower ratio indicates that a higher

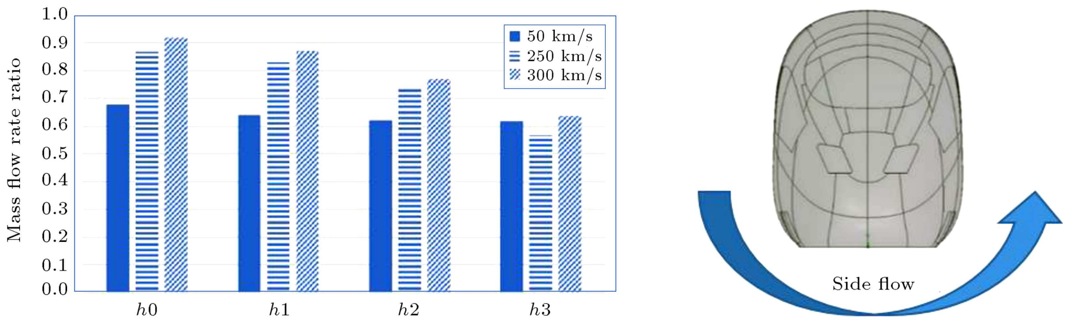

Figure 12. Schematic image of the side flow of the flow under the train in $(\frac{\dot{m}_5}{\dot{m}_3})$.

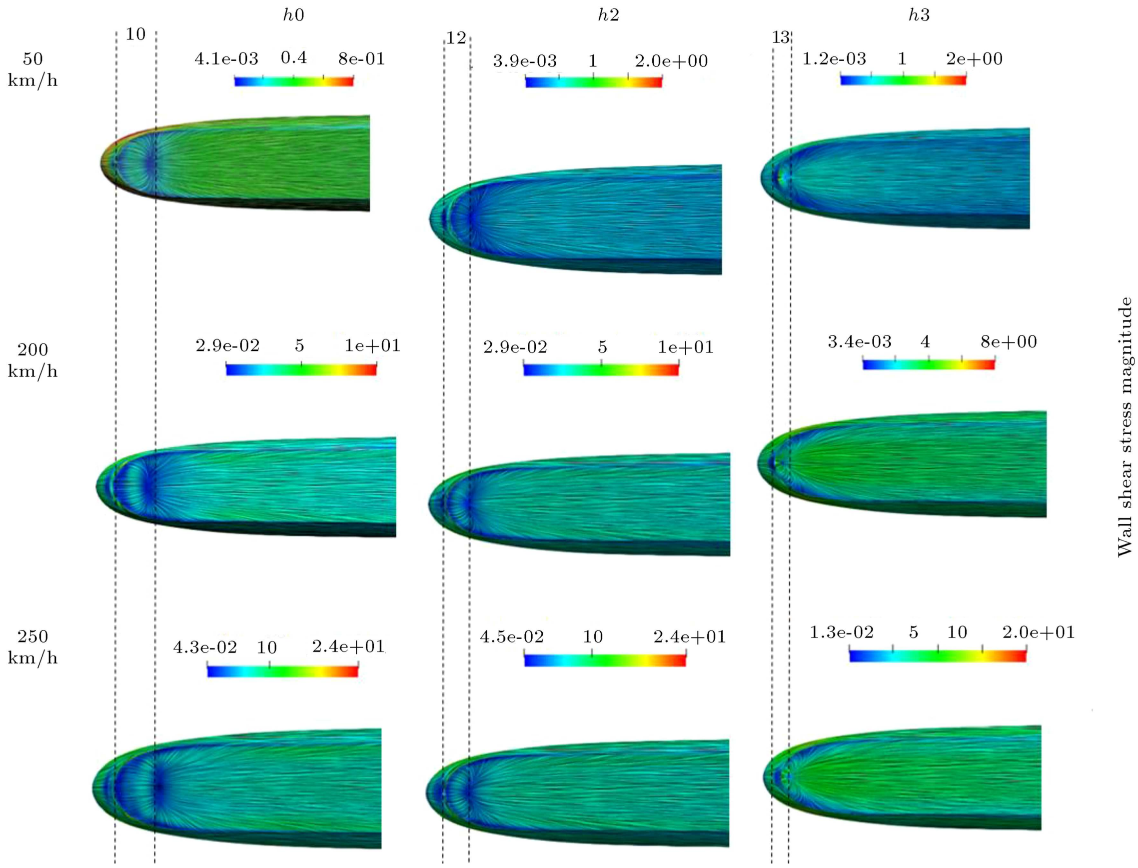

Figure 13. Shear stress and time-averaged trace lines in the front area of the train floor.

percentage of air under the train is inclined to both sides of the train and exits on both sides, as shown in Figure 12. Two significant reasons for this are the reduction of the cross-section of the passing air and the speed reduction at shorter distances. The only exceptions for this section are for speeds of 50 km/h and case h_3, where the flow rate has increased by 3%. In [3], similar results were obtained. Figure 12 shows that as the train speed increased, this speed ratio firstly increased. For example, at h_0 for 50 km/h, this ratio is 0.68. At 250 km/h, this ratio is 0.91, implying that a small percentage of the air under the train inclines to both sides. Therefore, less side flow is generated. This can be attributed to the air being drawn around the train to the mainline of the flow below the train at higher speeds.

The results reveal that although the most negative lift force is at h_3, the maximum air flow velocity under the train increases substantially compared to other distances. Former relevant studies have demonstrated that this increase in speed can upset the balance of passengers as well as pedestrians and workers around the train. Therefore, it seems that the distance h_3 is also problematic in this regard. Hence, the best distance seems to be h_2 considering all conditions (For further research, it is necessary to consider the cross-wind effects and more precise geometry.)

Figure 13 displays the shear stress contour generated on the train floor and time-averaged trace lines in the train head area for different cases. In front of the train, there is a separation zone caused by the panel installed in the front of the train. As the ground clearance decreases, the length of this bubble-like region relative to case h_0 decreases by 32% and 58%, respectively, which are named l2 and l3 in Figure 13, respectively. Given this separation bubble, the maximum dimensionless velocity increases below this area (Figure 11).

Figure 13 indicates that as the train speed increases, the length of the separation zone does not undergo significant changes, and this zone is affected the most by the ground clearance. However, as the train speed rises, the shear stress induced on the train floor increases.

One of the substantial ratios considered in the study of air flow around the train is the amount of air that deviates from that under the train to both sides of the train. By examining the mass flow of air in the two initial and final sections of the train and obtaining their ratio, it is determined how much air has come out from beneath the train to both sides. As can be seen in the figures, in this regard, longer distances (h_0) have the highest value, i.e., the flow rates of sections 5 and 3 are closer to each other. In other words, it has the least amount of exhaust air from around the train. However, as shown in Figure 13, at speeds above 250 km/h, the air outlet at h_2 is approximately 15% higher than that at h_0.

Based on examining the shear stress and the separation bubble zone under the train, it is concluded that reducing the ground clearance decreases the size of this bubble zone. Moreover, it is observed that with increasing speed, the size of this separation zone is not affected much, although the amount of shear stress increases significantly, which should be taken into account in determining the alloy utilized (in terms of strength) in the nose area of the train.

4. Conclusion

In this research, the effect of high-speed train speed and train ground clearance at five train speeds of 50, 150, 200, 250, and 350 km/h and, also, ground clearances of 0.048, 0.092, 0.136, and 0.22 for the train's height was numerically simulated utilizing the Unsteady $k-\omega$ SST turbulence model. The comparison of the results acquired by the Unsteady Reynolds-Averaged Navier-Stokes (URANS) method with laboratory results and those of high-order methods indicated that the $k-\omega$ SST model exhibited viable performance in predicting lift and drag forces. The train under consideration in this paper was the Inter-City-Express 3 (ICE3) train. In this paper, to assess the stability and make a balance between trains and passengers, the aerodynamic coefficients of lift and drag as well as air flow velocity profiles under the train were investigated.

Based on the examinations conducted and comparison made at different speeds, it was inferred that at all distances, regarding drag forces, the speed of 250 km/h could be considered critical to keeping the drag coefficient constant, considering the curvature of the graph and since the difference in the total drag coefficient at the last two speeds is less than 5%. It appears that in terms of lift forces, the distance h_1 is a limit distance. This implies that no matter how much the train speed increases up to this distance, the negative lift coefficient does not undergo tangible changes. Having said that, as this distance expands further, by increasing the speed (or, possibly, the effect of cross-wind or crossing the tunnel), the lift coefficients will rise and can cause the train to lift off the rails. This information can help determine the train speed range in a range of ground clearances.

It was discovered that with an increase in velocity at different distances, the contribution of pressure and friction components in the drag coefficient did not change significantly. In contrast, by reducing the ground clearance at different speeds, the ratio of frictional forces to pressure forces increased up to 4.5 times. The profile of air flow velocities under the train indicated an increase in the dimensionless speed as the ground clearance rose at different speeds, except in the front area of the train. This increase was specifically seen at a speed of 350 km/h and led to a 29% increase in the mentioned velocity along the sections under the train. This increase in speed could upset the balance of passengers and pedestrians as well as workers around the train.

References

1. Meng, S., Zhou, D., and Tan, C. "The effect of concave size on the aerodynamics of a Maglev train", *Journal of Bionic Engineering*, **19**(3), pp. 709–723 (2022).
2. Dong, T., Minelli, G., Wang, J., et al. "The effect of ground clearance on the aerodynamics of a generic high-speed train", *Journal of Fluids and Structures*, **95**, p. 102990 (2020).
3. Dong, T., Minelli, G., Wang, J., et al. "Numerical investigation of a high-speed train underbody flows: Studying flow structures through large-eddy simulation and assessment of steady and unsteady Reynolds-averaged Navier-Stokes and improved delayed detached eddy simulation performance", *Physics of Fluids*, **34**(1), p. 015126 (2022).
4. Du, H., Zhou, D., Meng, S., et al. "Effect of vortex generators on the aerodynamic performance of high-speed trains", *Flow, Turbulence and Combustion*, **109**(3), pp. 627–645 (2022).
5. Liu, Z., Zhang, X., Chen, T., et al. "Aerodynamic loads and bridge responses under train passage: case

study of an overpass steel box-girder cable-stayed bridge", *Advances in Bridge Engineering*, **3**(1), pp. 1–25 (2022).

6. Khorsandi, Z., Afshinpour, M., Molaei, F., et al. "Design and synthesis of novel phe-phe hydroxyethylene derivatives as potential coronavirus main protease inhibitors", *Journal of Biomolecular Structure and Dynamics*, **30**, pp. 1–9 (2021).

7. Ghalandari, M., Ziamolki, A., and Mosavi, A. "Aeromechanical optimization of first row compressor test stand blades using a hybrid machine learning model of genetic algorithm, artificial neural networks and design of experiments", *Engineering Applications of Computational Fluid Mechanics*, **13**(1), pp. 892–904 (2019).

8. Wickramasinghe, K. "The use of deep data locality towards a Hadoop performance analysis framework", *International Journal of Communication and Computer Technologies*, **8**(1), pp. 5–8 (2020).

9. Yang, W., Yue, H., Deng, E., et al. "Comparison of aerodynamic performance of high-speed train driving on tunnel-bridge section under fluctuating winds based on three turbulence models", *Journal of Wind Engineering and Industrial Aerodynamics*, **228**, 105081 (2022).

10. Li, T., Liang, H., Zhang, J., et al., "Numerical study on aerodynamic resistance reduction of high-speed train using vortex generator", *Engineering Applications of Computational Fluid Mechanics*, **17**(1), e2153925 (2023).

11. Li, T., Hemida, H., Rashidi, M.M., et al. "The effect of numerical divergence schemes on the flow around trains", *Fluid Dynamics Research*, **52**(2), p. 025509 (2020).

12. Johnson, M., Wagner, C., and Loose, S. "Particle image velocimetry of the underfloor flow for generic high-speed train models in a water towing tank", *Proceedings of the Institution of Mechanical Engineers, Part F: Journal of Rail and Rapid Transit*, **228**(2), pp. 194–209 (2014).

13. Premoli, A., Rocchi, D., Schito, P., et al. "Ballast flight under high-speed trains: Wind tunnel full-scale experimental tests", *Journal of Wind Engineering and Industrial Aerodynamics*, **145**, pp. 351–361 (2015).

14. Li, R., Xu, P., Peng, Y., et al. "Multi-objective optimization of a high-speed train head based on the FFD method", *Journal of Wind Engineering and Industrial Aerodynamics*, **152**, pp. 41–49 (2016).

15. Zhang, J., Li, J.J., Tian, H.Q., et al. "Impact of ground and wheel boundary conditions on numerical simulation of the high-speed train aerodynamic performance", *Journal of Fluids and Structures*, **61**, pp. 249–261 (2016).

16. Wang, S., Bell, J.R., Burton, D., et al. "The performance of different turbulence models (URANS, SAS, and DES) for predicting high-speed train slipstream", *Journal of Wind Engineering and Industrial Aerodynamics*, **165**, pp. 46–57 (2017).

17. Niu, J., Zhou, D., and Wang, Y. "Numerical comparison of the aerodynamic performance of stationary and moving trains with or without windbreak wall under cross-wind", *Journal of Wind Engineering and Industrial Aerodynamics*, **182**, pp. 1–15 (2018a).

18. Niu, J., Wang, Y., Zhang, L., et al. "Numerical analysis of aerodynamic characteristics of high-speed train with different train nose lengths", *International Journal of Heat and Mass Transfer*, **127**, pp. 188–199 (2018b).

19. Mohebbi, M. and Rezvani, M.A. "Analysis of the effects of lateral wind on a high speed train on a double routed railway track with porous shelters", *Journal of Wind Engineering and Industrial Aerodynamics*, **184**, pp. 116–127 (2019).

20. Noguchi, Y., Suzuki, M., Baker, C., et al. "Numerical and experimental study on the aerodynamic force coefficients of railway vehicles on an embankment in crosswind", *Journal of Wind Engineering and Industrial Aerodynamics*, **184**, pp. 20–105 (2019).

21. Zhao, Q., Chen, Z.H., Huang, Z.G., et al. "Optimization of the aerodynamic configuration of a tubular projectile based on blind kriging", *Scientia Iranica*, **26**(1), pp. 311–322 (2019).

22. Singh, R., Mehbodniya, A., Webber, J.L., et al. "Analysis of network slicing for management of 5G networks using machine learning techniques", *Wireless Communications and Mobile Computing*, **2022**, p. 9169568, (2022).

23. Nejati, M., Shokrollahi, S., Shams, S., et al. "A modified indicial functions approximation for nonlinear aeroelastic analysis", *Scientia Iranica*, **27**(3), pp. 1230–1254 (2020).

24. Malli, K., Nerella, A., Sri, K., et al. "Design of clocked jk flip flop using air hole structured photonic crystal", *Journal of VLSI Circuits and Systems*, **3**(2), pp. 11–20 (2021).

25. Srinivasareddy, S., Narayana, Y.V., and Krishna, D. "Sector beam synthesis in linear antenna arrays using social group optimization algorithm", *National Journal of Antennas and Propagation*, **3**(2), pp. 6–9 (2021).

26. Rakshe, S., Nimje, S.V., and Panigrahi, S.K. "Optimization of adhesively bonded Spar-Wingskin joints of laminated FRP composites subjected to pull-off load: A critical review", *Reviews of Adhesion and Adhesives*, **8**(1), pp. 29–46 (2021).

27. Band, S.S., Al-Shourbaji, I., Karami, H., et al. "Combination of group method of data handling (GMDH) and computational fluid dynamics (CFD) for prediction of velocity in channel intake", *Applied Sciences*, **10**(21), p. 7521 (2020).

28. Patil, S., Bhosale, A., Dhepe, V., et al. "Impact energy absorption capability of polygonal cross-section

thin-walled beams under lateral impact", *International Journal of Innovative Research and Scientific Studies*, **4**(4), pp. 205–214 (2021).

29. Lv, D., Niu, J., and Yao, H. "Numerical study on transient aerodynamic characteristics of high-speed trains during the opening of braking plates based on dynamic-overset-grid technology", *Journal of Wind Engineering and Industrial Aerodynamics*, **233**, 105299 (2023).

30. Moshahedi, A. and Mehranfar, N. "A comprehensive design for a manufacturing system using predictive fuzzy models", *Journal of Research in Science, Engineering and Technology*, **9**(3), pp. 1–23 (2021).

31. Mehbodniya, A., Douraki, B.K., Webber, J.L., et al. "Multilayer reversible data hiding based on the difference expansion method using multilevel thresholding of host images based on the slime mould algorithm", *Processes*, **10**(5), p. 858 (2022).

32. Timnak, N., Jahangirian, A., and Seyyedsalehi, S.A. "An optimum neural network for evolutionary aerodynamic shape design", *Scientia Iranica*, **24**(5), pp. 2490–2500 (2017).

33. Muñoz-Paniagua, J., García, J., and Crespo, A. "Genetically aerodynamic optimization of the nose shape of a high-speed train entering a tunnel", *Journal of Wind Engineering and Industrial Aerodynamics*, **130**, pp. 48–61 (2014).

34. Xia, C., Wang, H., Shan, X., et al. "Effects of ground configurations on the slipstream and near wake of a high-speed train", *Journal of Wind Engineering and Industrial Aerodynamics*, **168**, pp. 177–189 (2017).

35. Munoz-Paniagua, J. and García, J. "Aerodynamic drag optimization of a high-speed train", *Journal of Wind Engineering and Industrial Aerodynamics*, **204**, 104215 (2020).

36. Ma, Y., Zhang, B., Frenkel, I., et al. "Mussel-inspired underwater adhesives-from adhesion mechanisms to engineering applications: A critical review", *Reviews of Adhesion and Adhesives*, **9**(2), pp. 167–187 (2021).

Biographies

Sajjad Norouzi is the PhD candidate at the Department of Mechanical Engineering, Sahand University of Technology, Tabriz, Iran. His research interests are aerodynamic, fluid mechanics, and optimization. Now, he is working on his PhD thesis in aerodynamic performance of the high-speed trains and its optimization.

Siamak Hossainpour is a Professor in Mechanical Engineering at Sahand University of Technology, Tabriz, Iran. He received his BSc degree in Mechanical Engineering from Sharif University of Technology, Tehran, Iran, followed by MSc and PhD degrees from the Mechanical Engineering Department of this University. He presented and contributed to more than 60 papers at various international and national journals and conferences. His research interests involve computational fluid dynamics, convection in porous medium, heat transfer enhancement, renewable energy, and Co_2 capture and storage.

Mohammad Mehdi Rashidi was a highly cited researcher in the year 2018, 2019, and 2020. He has published over 345 journal papers indexed in Scopus and Web of Science (h-index=72) and 50 conference papers. He was an Honorary Fellow at the Australian Institute of High Energetic Materials. His papers have been published in Nature, Nano Energy, Applied Thermal Engineering, and Energy journals. His research interests include heat and mass transfer, multiphase flows, micro fluidics, computational fluid dynamics, and drug delivery.